Ce_{3-x}Mg_{x}Co_{9}: Transformation of a Pauli Paramagnet into a Strong Permanent Magnet

Tej N. Lamichhane, Valentin Taufour, Andriy Palasyuk, Qisheng Lin, Sergey L. Bud'ko, and Paul C. Canfield

Phys. Rev. Applied **9**, 024023 — Published 23 February 2018

DOI: 10.1103/PhysRevApplied.9.024023

$Ce_{3-x}Mg_xCo_9$: transformation of a Pauli paramagnet into a strong permanent magnet

Tej N. Lamichhane,[1,2] Valentine Taufour,[1,3] Andriy Palasyuk,[1]
Qisheng Lin,[1] Sergey L. Bud'ko,[1,2] and Paul C. Canfield[1,2]

[1] *Ames Laboratory, U.S. DOE, Ames, Iowa 50011, USA*
[2] *Department of Physics and Astronomy, Iowa State University, Ames, Iowa 50011, USA*
[3] *Department of Physics, University of California Davis, Davis, California 95616, USA*

We report on the synthesis of single crystalline and polycrystalline samples of $Ce_{3-x}Mg_xCo_9$ solid solution ($0 \leq x \lesssim 1.4$) and characterization of their structural and magnetic properties. The crystal structure remains rhombohedral in the whole composition range and Mg partially replaces Ce in the $6c$ site of the $CeCo_3$ structure. Ferromagnetism is induced by Mg substitutions starting as low as $x = 0.18$ and reaching a Curie temperature as high as 450 K for $x = 1.35$. Measurements on single crystals with $x = 1.34$ and $T_C = 440$ K indicate an axial magnetic anisotropy with the anisotropy field of 6 T and a magnetization of 6 μ_B/f.u. at 300 K. Coercicity is observed in the polycrystalline samples consistent with the observed axial magnetic anisotropy. Our discovery of ferromagnetism with large axial magnetic anisotropy induced by substituting a rare-earth element by Mg is a very promising result in the search of inexpensive permanent-magnet materials and suggests other non-magnetic phases, similar to $CeCo_3$, may also conceal nearby ferromagnetic phases.

I. INTRODUCTION

Current rare-earth-based commercial magnets contain local moment bearing rare-earth elements, mainly Nd, Sm and Dy whose availability is, according to the United States Department of Energy, important to the clean energy economy and also have an associated supply risk. Alternative to finding a long sought rare earth free, high flux permanent magnet, attempts to find Ce-based permanent magnets or substituting Ce for more critical rare-earth elements could be a pragmatic strategy to address the criticality problem since Ce is a relatively more abundant rare earth [1] with easier extraction chemistry. Ce is relatively easy to separate from the other rare earths since it can easily be oxidised to CeO_2 via roasting from which it can be precipitated out in acidic solutions [2, 3]. Ce can be, in theory as well as experiment, a substitute for critical rare-earths without much compromise in magnetic properties [4]. Because of the volatile price of critical rare-earths, Ce is drawing attention for developing gap-magnets which will populate the gap in energy product (in the range of 10-20 MGOe) in between low flux (Alnico, ferrites) and commercial rare-earth based magnets such as $SmCo_5$ and $Nd_2Fe_{14}B$. Additionally, the study of new Ce based compounds often can reveal interesting physics; Ce exhibits diverse electronic and magnetic properties like local moment bearing Ce^{3+} ion, non-magnetic Ce^{4+} ion, mixed valency, intermediate valence and itinerant magnetism.

$Ce_{3-x}Mg_xCo_9$ alloys are substitution derivatives of $CeCo_3$ in which Mg partially replace Ce in the $6c$ position. The hydrogenation properties of the compound Ce_2MgCo_9 ($x = 1$) and $Nd_{3-x}Mg_xCo_9$ alloys ($x \leq 1.5$) have been recently investigated [5, 6]. In addition, it was shown that the substitution of Nd by Mg increases the Curie temperature from 381 K for $NdCo_3$ [7] to 633 K for Nd_2MgCo_9 [6].

In this work we present structural and magnetic properties of both single crystalline and polycrystalline $Ce_{3-x}Mg_xCo_9$ for $0 \leq x \lesssim 1.4$. The anisotropic magnetic properties are studied for a single crystal of $Ce_{1.662(4)}Mg_{1.338(4)}Co_9$ (Hereafter we round off the single crystalline composition to 3-significant digits as $Ce_{1.66}Mg_{1.34}Co_9$.). We find a remarkable transformation of a Pauli-paramagnet $CeCo_3$ (Ce_3Co_9) into the potential permanent magnet $Ce_{3-x}Mg_xCo_9$ which develops 2.2 MJ/m^3 of uniaxial anisotropy energy at 2 K for the $Ce_{1.66}Mg_{1.34}Co_9$.

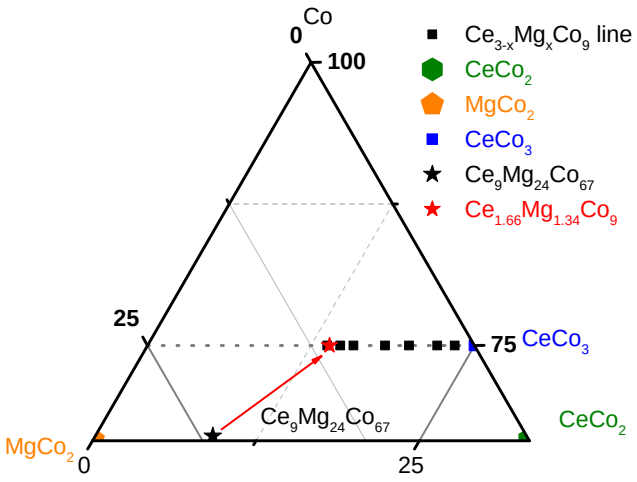

Figure 1. Co-rich portion of the Co-Mg-Ce ternary phase diagram showing the $Ce_{3-x}Mg_xCo_9$ solid solution line and 1:2 type impurity phases. $Ce_9Mg_{24}Co_9$ is the optimised initial melt composition for the solution growth of single crystalline $Ce_{1.66}Mg_{1.34}Co_9$. (See text for details.)

II. EXPERIMENTAL METHODS

To establish the existence range of the solid solution $Ce_{3-x}Mg_xCo_9$, we prepared polycrystals with various nominal compositions of $0 \leq x \leq 2.00$ (see TABLE III below). Ce metal from the Ames Laboratory Material Preparation Center (purity > 99.99%), Co chunks (99.95%, Alfa Aesar), and Mg (99.95%,Gallium Source, LLC) were packed in a 3-capped Ta crucible [8] under an Ar atmosphere. The Ta crucible was then sealed into an amorphous silica ampoule. The ampoule was heated to 900 °C over 3 hours and held there for 3 hours. This step allows the reaction of Ce and Mg at low temperature and avoids the excessive boiling of Mg inside the Ta crucible. The ampoule was then heated to 1200 °C over 3 hours and held there for 10 hours. At this point, the ampoule was spun in a centrifuge and all the molten growth material was decanted and quenched in catch side of the Ta-tube. This step confirmed that the mixture was forming a homogeneous melt at 1200 °C. The ampoule was put back into a furnace then annealed at 900 °C for 24 hours. Mg free $CeCo_3$ was also synthesized by arcmelting the stoichiometric composition and annealing at 900 °C for 1 week.

Single crystals of $Ce_{3-x}Mg_xCo_9$ were grown using a solution growth technique. An initial composition of $Ce_9Mg_{24}Co_{67}$ (see FIG. 1) was packed in a 3-capped Ta crucible [8] and heated to 1200 °C similar to the polycrystals. The ampoule was then cooled down to 1100 °C over 75 hours after which crystals were separated from the flux by using a centrifuge. Similarly, $CeCo_3$ single crystals were prepared by cooling a $Ce_{30}Co_{70}$ melt from 1200° to 1100 °C in 1 hour and then to 1050 °C over 75 hours[9].

Elemental analysis of the samples was performed using Energy Dispersive Spectroscopy(EDS). Polycrystalline samples were embedded in epoxy resin and finely polished. The polished samples were examined with EDS on 6-10 spots and a statistical average composition is reported. Thin plate-like single crystalline samples, see FIG. 2(a), were mounted on a conducting carbon tape. Self-flux grown $MgCo_2$ and $CeCo_2$ single crystals were used as absorption standards for the Ce-Co-Mg alloy composition analyses. Powder X-ray diffraction data were collected at room temperature on a Rigaku Mini-Flex II diffractometer with Cu Kα radiation. Data were collected with a 3 seconds dwell time for each interval of 0.01° within a 2θ range of $10 - 100°$. Lattice parameters were refined by the Rietveld analysis method using GSAS [10] and EXPGUI [11].

Single crystal X-ray diffraction was carried out on a Bruker Smart APEX II diffractometer with graphite-monochromatized Mo-K_α radiation (0.71073 Å). Reflections were gathered at room temperature by taking four sets of 360 frames with 0.5° scans in ω, with an exposure time of 10 s. The crystal-to-detector distance was maintained 60 mm. The reflections were collected over the range of 3° to 62° in 2θ.

Electrical resistivity was measured on single crystals using the 4-probe technique with a Linear Research, Inc. ac resistance bridge (LR700, f = 17 Hz). A Quantum Design (QD) Magnetic Property Measurement System (MPMS) was used for the temperature control. Samples were sliced into thin rectangular bars (approximately 0.9 mm x 0.45 mm x 0.04 mm) and platinum wires were attached to the samples with Dupont 4929N silver paint. The contact resistances were less than 2 Ω.

Magnetization was measured using a QD-VersaLab Vibrating Sample Magnetometer (VSM). The standard option was used in the temperature range 50-400 K and the oven option in the range 300-1000 K. Loctite 435 and Zircar cement were used to attach the samples in the standard and oven options, respectively. Field dependent magnetization isotherms were also measured down to 2 K in a MPMS. The details of sample mounting and experimental determination of demagnetization factor along the easy axis are discussed in references 12 and 13.

III. COMPOSITION AND STRUCTURAL PROPERTIES

1. *Single crystal: Characterization and structure*

Table I. Crystallographic data and refinement parameters for $Ce_{1.662(4)}Mg_{1.338(4)}Co_9$.

Empirical formula	$Ce_{1.662(4)}Mg_{1.338(4)}Co_9$
Formula weight	796.32
Crystal system, space group	trigonal, *R-3m* h
Unit cell dimensions	$a = 4.9260(7)$ Å
	$c = 24.019(5)$ Å
Volume	504.75(18) Å^3
Z, Calculated density	3, 7.859 g/cm^3
Absorption coefficient	32.577 mm^{-1}
Reflections collected	2000 [$R_{(int)} = 0.0408$]
Data / restraints / parameters	224 / 0 / 18
Goodness-of-fit on $\|F\|^2$	1.149
Final R indices [$I > 4\sigma(I)$]	$R1 = 0.0204$, $wR2 = 0.0450$
R indices (all data)	$R1 = 0.0226$, $wR2 = 0.0455$
Largest diff. peak and hole	1.917 and -1.477 e.Å^{-3}

A picture of as grown $Ce_{1.66}Mg_{1.34}Co_9$ single crystals, a Laue backscattered photograph and single crystal surface diffracted monochromatic XRD data collected via Rigaku MiniFlex II diffractrometer with Bragg-Brentano geometry [14] are presented in pannels (a), (b) and (c) of FIG. 2 respectively. Both Laue and monochromatic single crystalline XRD data confirmed that the single crystals grow with a planar morphology with the c-axis perpendicular to the plates.

The crystallographic data obtained from the single crystal X-ray diffraction for $Ce_{1.66}Mg_{1.34}Co_9$ grown out

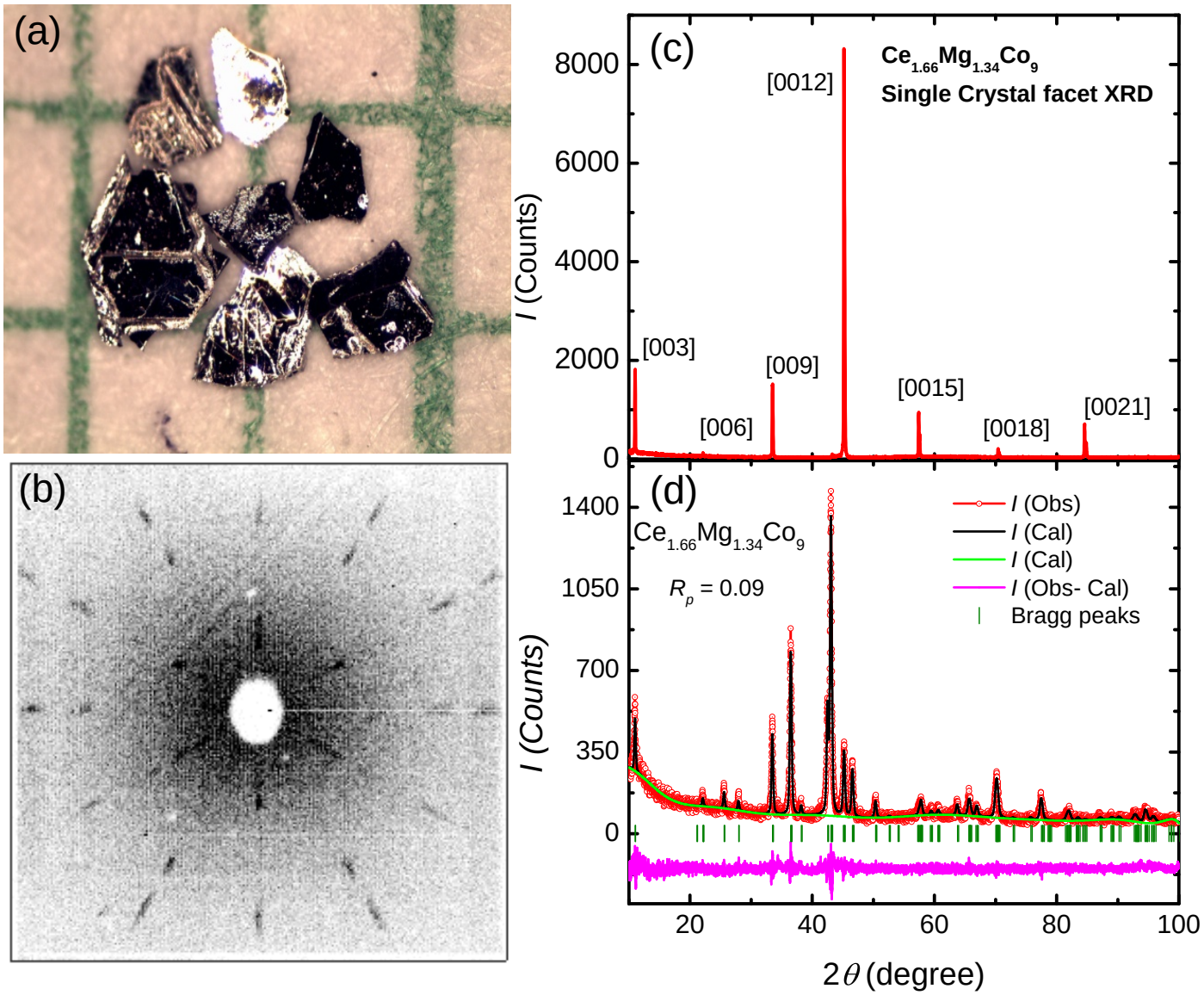

Figure 2. (a) Single crystals of $Ce_{1.66}Mg_{1.34}Co_9$. (b) Backscattered Laue photograph of $Ce_{1.66}Mg_{1.34}Co_9$ with X-ray beam perpendicular to plate. (c) Monochromatic X-ray diffraction from the surface of single crystal using Bragg-Brentano geometry. (d) Powder XRD for $Ce_{1.66}Mg_{1.34}Co_9$ where I(Obs), I(Cal) and I(Bkg) are experimental, Rietveld refined and instrumental background data respectively. The lower section of the graph shows the Bragg's peaks positions with olive vertical lines and the differential X-ray diffractrogram I(Obs-Cal).

Table II. Atomic coordinates and equivalent isotropic displacement parameters ($Å^2 \times 10^{-3}$) for $Ce_{1.66}Mg_{1.34}Co_9$. $U_{(eq)}$ is defined as one third of the trace of the orthogonalized U_{ij} tensor.

atom	Wyckoff site	Occ	x	y	z	U_{eq}
Ce(1)	$3a$	1	0	0	0	14(1)
Ce(2)	$6c$	0.338 (4)	0	0	0.1414(1)	12(1)
Mg(2)	$6c$	0.662 (4)	0	0	0.1414(1)	12(1)
Co(1)	$3b$	1	0	0	$\frac{1}{2}$	11(1)
Co(2)	$6c$	1	0	0	0.3339(1)	17(1)
Co(3)	$18h$	1	0.5014(1)	0.4986(1)	0.0840(1)	11(1)

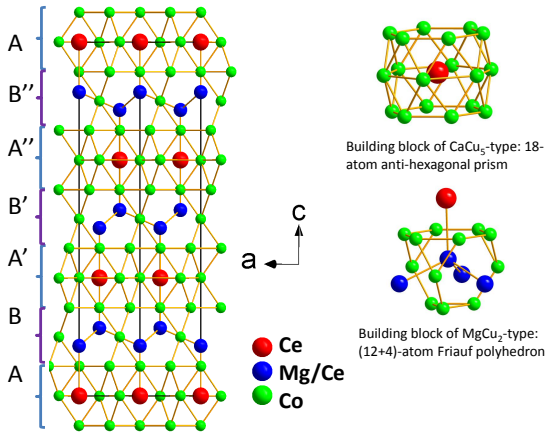

Figure 3. The crystal structure for $Ce_{3-x}Mg_xCo_9$ showing the stacking sequence of $CaCu_5$ type plane (A) and $MgCu_2$ type plane (B) visualized along [010] direction.

of $Ce_9Mg_{24}Co_{67}$ initial melt are summarized in TABLES. I, and II. FIG. 2(d) shows a powder X-ray diffraction pattern of the crushed single crystals which has some noticeable mismatch in observed and Rietveld refined intensity of {00l} families of the peaks, indicating a degree of preferred orientation in the powder sample. As mentioned above, the relatively small crystal size made it difficult to acquire enough powder sample to obtain less noisy XRD data and better statistics in the Rietveld refinement. To reduce the intensity mismatch, a preferred orientation correction was employed in the Rietveld refinement using spherical harmonics up to 12^{th} order and absorption correction for plate like grains in the powder sample. The Rietveld refined lattice parameters for powder XRD data of the single crystal $Ce_{1.66}Mg_{1.34}Co_9$ are $a = 4.923(1)$ $Å$ and $c = 24.026(1)$ $Å$ with $R_p = 0.09$ which are in close agreement (within 2-3σ) with single crystal XRD data as shown in TABLE I. The single crystal XRD composition was $Ce_{13.92}Mg_{11.08}Co_{75}$ ($Ce_{1.662(4)}Mg_{1.338(4)}Co_9$). Although we did not make quantitative compositional analysis measurement on the single crystalline sample with EDS (The crystals were too thin to readily polish and small droplets of Mg rich flux was on their surfaces.) we could detect the minor presence of Ta, (up to 1 at.%) most likely caused by slight dissolution of the inner wall surfaces of Ta reaction container and diffusion of Ta atoms into the reaction liquid during the long term dwelling process at the maximum temperature of 1200° C as well as at ramping down to 1100° C over 75 hours. However, an attempt to solve the crystal structure along with inclusion of Ta in any Wyckoff sites or interstitial sites was unsuccessful. We believe that Ta is distributed in our crystals in the form of nano-sized precipitates rather than incorporated into interstices of the crystals structure.

The crystal structure of $Ce_{3-x}Mg_xCo_9$ is rhombohedral and belongs to the $PuNi_3$ type structure[5]. Similar to the $R_{3-x}Mg_xNi_9$ series, the Co-containing structure is an intergrowth of $CaCu_5$-type (A) and $MgCu_2$-type (B) building blocks with a repeating sequence of ABA'B'A"B"A as shown in FIG. 3. Here A', B' and A", B" are introduced to show the relative translation of the growth layers with respect to c-axis during stacking. There are two independent sites for Ce atoms in this structure: one $3a$ site is located at the center of a face-shared anti-hexagonal prism defined by 18 Co atoms; the other $6c$ site is surrounded by 12 Co atoms defining a truncated tetrahedron plus four capping atoms at longer distances. As expected from the polyhedra volume, the statistically distributed Ce/Mg mixtures prefer to occupy the Wyckoff $6c$ site with its smaller volume.

2. *Polycrystalline samples: Composition and lattice parameters*

The nominal and EDS composition of the polycrystalline samples are presented in TABLE III along with the Rietveld refined percentage of the majority phase in the sample. The SEM images for mixed and predominantly single phase $Ce_{3-x}Mg_xCo_9$ samples are presented in FIG. 4. Panel (a) in FIG. 4 shows the mixed phase sample that forms out of a nominal composition $Ce_{2.25}Mg_{0.75}Co_9$ and the panel (b) shows the predominantly single phase sample with EDS composition $Ce_{1.89}Mg_{1.11}Co_9$. In addition TABLE III summarizes phase analysis based on powder XRD data.

The crystallographic information file obtained from single crystal XRD was used to perform Rietveld refinement of the powder XRD data of polycrystal samples listed in TABLE III. Rietveld refined XRD patterns for a multiple phase polycrystalline samples (Nominal $Ce_{2.75}Mg_{0.25}Co_9$ with $R_p = 0.09$ and $Ce_{2.50}Mg_{0.50}Co_9$ with $R_p = 0.10$) and single phase polycrystalline $Ce_{1.89}Mg_{1.11}Co_9$ (EDS composition) with $R_p = 0.08$ are presented in FIG. 5, 6 and 7 respectively. The

Table III. The comparison of the loaded compositions with the EDS determined composition. A nominal presence of Ta (up to 1 at.%) was found in the homogeneous $Ce_{3-x}Mg_xCo_9$ samples. Some of the higher-Mg samples showed traces of a $TaCo_3$ impurity phase and low-Mg content samples showed a $TaCo_2$ phase.

Loaded composition (Nominal)	EDS composition	Rietveld Refinement % of majority phase: $Ce_{3-x}Mg_xCo_9$
$CeCo_3$ (arcmelted and annealed at 900°C for 7 days)	$CeCo_3$ + $CeCo_2$	$\geq 88\%$
$Ce_{2.75}Mg_{0.25}Co_9$	$Ce_{2.82}Mg_{0.18}Co_9$ + $Ce_{0.86}Mg_{0.14}Co_2$ + $TaCo_2$	$\geq 67\%$
$Ce_{2.50}Mg_{0.5}Co_9$	$Ce_{2.66}Mg_{0.34}Co_9$ + $Ce_{0.77}Mg_{0.23}Co_2$	$\geq 76\%$
$Ce_{2.25}Mg_{0.75}Co_9$	$Ce_{2.40}Mg_{0.60}Co_9$ + $Ce_{0.80}Mg_{0.20}Co_2$	$\geq 80\%$
$Ce_2Mg_{1.0}Co_9$	$Ce_{2.18}Mg_{0.82}Co_9$	$\approx$ single phase
$Ce_{1.67}Mg_{1.33}Co_9$	$Ce_{1.89}Mg_{1.11}Co_9$	$\approx$ single phase
$Ce_{1.5}Mg_{1.5}Co_9$	$Ce_{1.77}Mg_{1.23}Co_9$	$\approx$ single phase
$Ce_{1.33}Mg_{1.67}Co_9$	$Ce_{1.65}Mg_{1.35}Co_9$	$\approx$ single phase
$CeMg_2Co_9$	$Ce_{1.42}Mg_{1.58}Co_9$ + $MgCo_2$ + Co	$\geq 50\%$

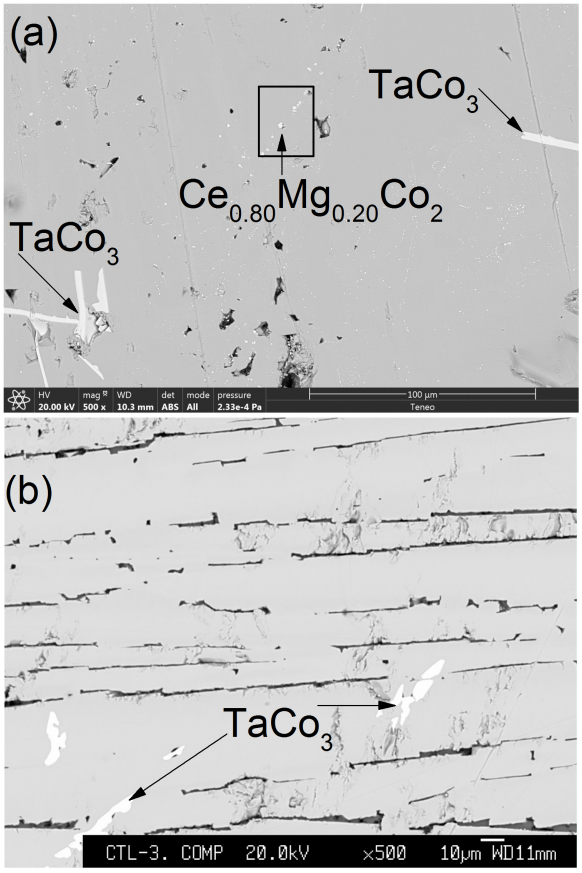

Figure 4. SEM images of mixed phase and predominantly single phase $Ce_{3-x}Mg_xCo_9$ samples (a) Nominal $Ce_{2.25}Mg_{0.75}Co_9$ which gave a mixture of $Ce_{2.40}Mg_{0.60}Co_9$ (majority phase) and $Ce_{0.80}Mg_{0.20}Co_2$ (minority phase demonstrated as faint small white spots along the diagonal of the black box in the panel (a)) and large white stripes of $TaCo_3$ impurity phase (b) Predominantly single phase $Ce_{1.89}Mg_{1.11}Co_9$ along with some traces of $TaCo_3$ impurity. The black parallel grooves in the image represent the cracks in the polished sample.

melt-annealed nominal $Ce_{2.75}Mg_{0.25}Co_9$ sample contains $\sim$ 67% of $Ce_{2.82}Mg_{0.18}Co_9$ phase, $\sim$ 23% of $Ce_{0.86}Mg_{0.14}Co_2$ and $\sim$ 10% of $TaCo_2$ inferred from Rietveld refinement. The $TaCo_2$ phase is not observed in the nominal $Ce_{2.50}Mg_{0.5}Co_9$ and higher content of Mg as shown in FIG. 6 and 7. An unidentified XRD peak was observed in nominal $Ce_{2.50}Mg_{0.50}Co_9$ sample as shown in FIG. 6 however $TaCo_2$ phase was almost reduced to zero in comparison to nominal composition $Ce_{2.75}Mg_{0.25}Co_9$ as shown in FIG. 5. But traces of $TaCo_3$ phase was observed in predominantly single phases $Ce_{3-x}Mg_xCo_9$ samples. These results combined with the fact that even pure (Mg = 0) $CeCo_3$ remains mixed phase after 7 days of annealing, suggest that Mg be assisting the annealing of polycrystalline $Ce_{3-x}Mg_xCo_9$ samples.

For nominal $x = 2$ and higher, $Ce_{3-x}Mg_xCo_9$ can no longer be considered a clear majority phase with the presence of the significant amount of $CoMg_2$ and Co. Looking at the composition of the $Ce_{3-x}Mg_xCo_9$ alloys from EDS, it seems that $x \approx 1.4$ is the maximum solid solubility. In the $Nd_{3-x}Mg_xCo_9$ alloys, the structure changes from the trigonal structure for $x \leq 1.5$ to a tetragonal structure at $x = 2$ (YIn_2Ni_9-type) [6]. The solubility range of Mg in $CeCo_3$ is therefore similar but we do not observe a phase corresponding with the YIn_2Ni_9-type structure for $x \geq 2$. Instead, a three phase region of $MgCo_2$, $Ce_{3-x}Mg_xCo_9$ and Co is observed (see TABLE III). The compositional range of our $Ce_{3-x}Mg_xCo_9$ samples is summarized in FIG. 1.

The variation of the polycrystalline lattice parameters and unit cell volume as a function of the Mg content in the $Ce_{3-x}Mg_xCo_9$ phase as determined from EDS is shown in FIG. 8. As expected, the substitution of Ce by Mg results in the reduction of the unit cell volume, similar to the case of $Nd_{3-x}Mg_xCo_9$ alloys [6]. Neither the a or c-lattice parameter follows a linear relation with Mg content x. The variation in a lattice parameter shows the slight positive deviation and c lattice parameter shows the slight negative deviation starting in the middle of the single phase region. The negative deviation of lattice parameter c might indicate that the covalent bonding is increased along that direction. It should be noted that the lattice parameters (a, c, v) and composition inferred from the single crystal X-rays (shown as corresponding color $\star$s) agree very well with what we inferred from EDS

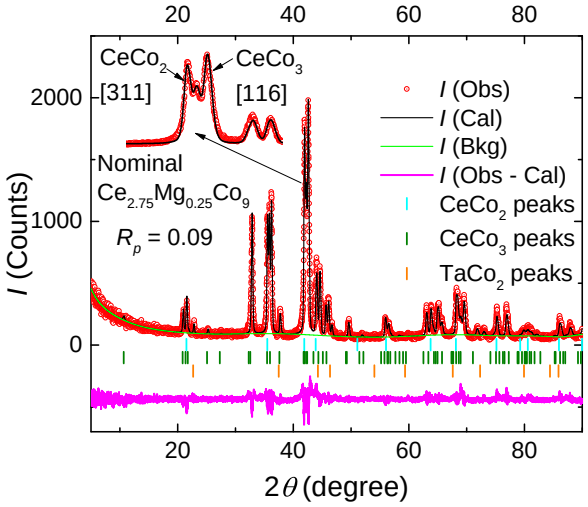

Figure 5. A typical example of multiphase polycrystalline XRD pattern for nominal $Ce_{2.75}Mg_{0.25}Co_9$ sample. The enlarged peak on the left top of the graph shows the broadening of the highest intensity peak of $Ce_{3-x}Mg_xCo_9$ around 2θ value of 42° due to presence of Mg doped $CeCo_2$ diffraction peak. I(Obs), I(Cal) and I(Bkg) are experimental, Rietveld refined and instrumental background data respectively. The lower section of the graph shows the Bragg's peaks positions with different coloured vertical lines for phases shown in the graph and the differential X-ray diffractrogram I(Obs-Cal).

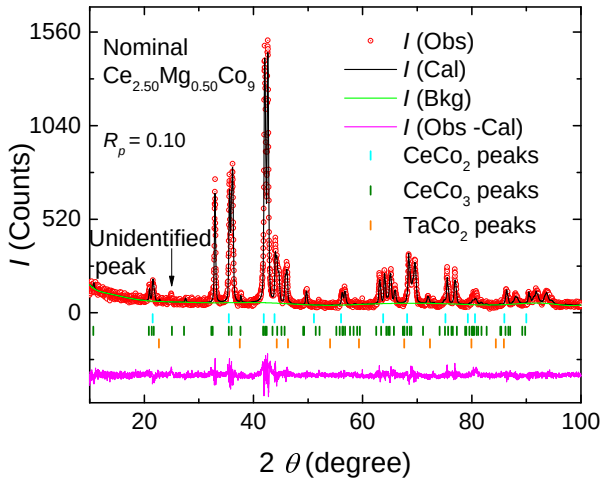

Figure 6. Powder XRD pattern for nominal $Ce_{2.50}Mg_{0.50}Co_9$ sample. $TaCo_2$ phase is almost not detectable for XRD however an unidentified XRD peak is observed around 2θ value of 25°. I(Obs), I(Cal) and I(Bkg) are experimental, Rietveld refined and instrumental background data respectively. The lower section of the graph shows the Bragg's peaks positions with different coloured vertical lines for phases shown in the graph and the differential X-ray diffractrogram I(Obs-Cal)

measurements on the polycrystalline samples.

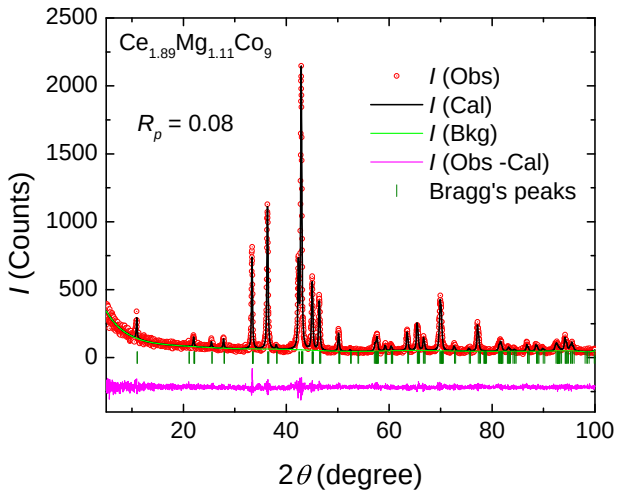

Figure 7. A typical example of predominantly single phase polycrystalline XRD pattern for EDS characterized $Ce_{1.89}Mg_{1.11}Co_9$ sample. I(Obs), I(Cal) and I(Bkg) are experimental, Rietveld refined and instrumental background data respectively. The lower section of the graph shows the Bragg's peaks positions with olive vertical lines and the differential X-ray diffractrogram I(Obs-Cal)

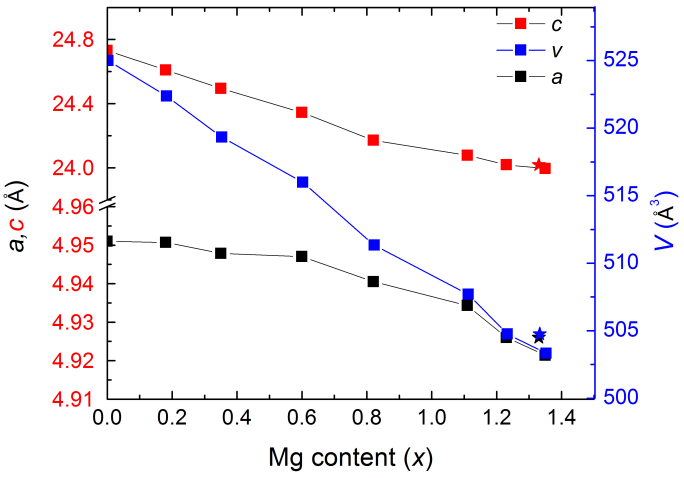

Figure 8. Variation of lattice parameters (a,c) and unit cell volume (v) of polycrystalline with Mg content inferred from EDS. Cubic $Ce_{1-x}Mg_xCo_2$ types impurity phases were obtained for $x \leq 0.6$ and predominant single phase $Ce_{3-x}Mg_xCo_9$ is obtained for $0.6 < x \leq 1.4$. The lattice parameters for single crystalline $Ce_{1.66}Mg_{1.34}Co_9$ are presented with corresponding color stars. The uncertainty in the refined lattice parameters is less than 0.01% of the reported lattice parameters and too small to clearly show as an error bar in the diagram.

IV. MAGNETIC PROPERTIES

Previously reported data do not agree about the magnetic properties of the parent compound, $CeCo_3$. Lemaire reported $CeCo_3$ as a ferromagnetic material with Curie temperature 78 K [15]. Buschow identified it as a

Pauli-paramagnetic phase however he left a room for further investigation mentioning $CeCo_3$ could be ferromagnetic below 10 K[16]. To clarify this issue, we measured the temperature dependent magnetization and electric resistivity of our single crystalline samples down to 2 K as shown in FIG. 9. The magnetization data shows no signature of a phase transition and is only weakly temperature dependent and is consistent with a Pauli-paramagnet and an impurity tail below 20 K. Assuming Curie tail is because of Ce^{3+} magnetic ions in the single crystalline $CeCo_3$ sample, magnetic susceptibility was fitted to Curie-Weiss law up to 150 K as:

$$\chi(T) = \chi_0 + \frac{C}{T-\theta}$$

where χ_0 is high temperature asymptotic susceptibility, C is Curie constant and θ is Curie-Weiss temperature. The concentration of Ce^{3+} ions was estimated to be $\sim 20\%$ (with $\theta = 3.8$ K) using the spin only moment of $2.54\mu_B$ per Ce^{3+} ion. The electrical resistivity does not show any signature of a loss of spin disorder scattering that would be anticipated for a magnetic phase transition.

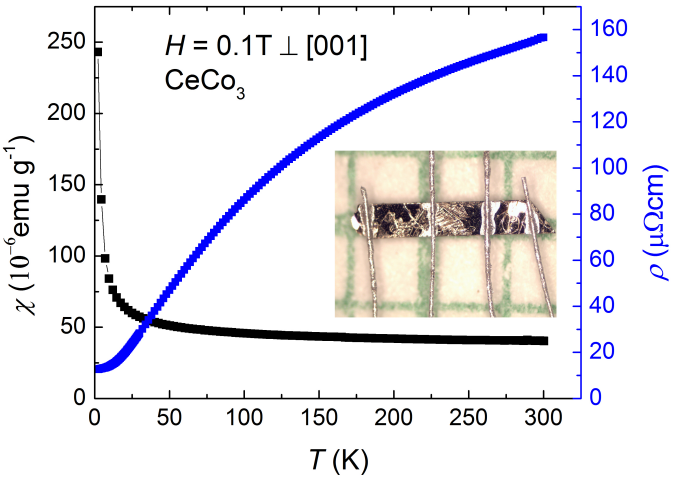

Figure 9. Temperature dependent susceptibility ($H = 0.1$ T $\perp$ [001]) and electrical resistivity (excitation current $\perp$ to [001]) of $CeCo_3$ single crystal. The picture in the inset shows the resistivity bar for four probe measurement. The sample was 60 micrometer thick.

The temperature dependence of the magnetization data of the single phase $Ce_{3-x}Mg_xCo_9$ polycrystalline samples are shown in FIG. 10. A rapid increase of the magnetization upon cooling below the Curie temperature is observed for $x = 0.82$ - 1.35 indicating the appearance of ferromagnetism with Mg substitution.

The Curie temperature T_C is estimated as the cross-point of linear extrapolations of two tangents to magnetization curve around the point of inflection as indicated on the curve $x = 1.11$ and $x = 1.23$ in FIG. 10. The variation of T_C with Mg substitution is shown in the inset. The Curie temperature increases with Mg concentration and reaches as high as 450 K for $x = 1.35$.

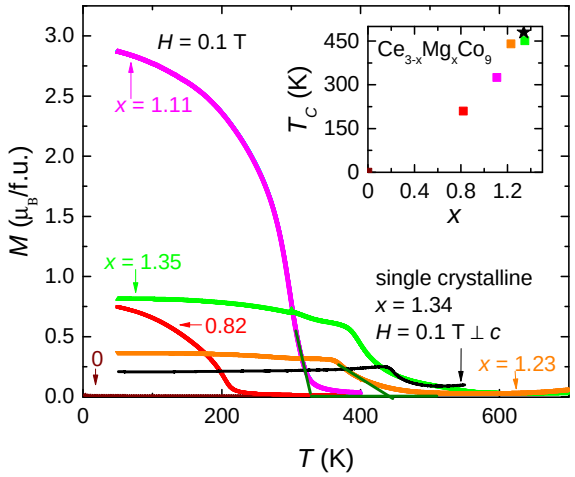

Figure 10. Temperature dependent magnetization of single crystalline ($x = 0$ and 1.34) polycrystalline $Ce_{3-x}Mg_xCo_9$ measured under a magnetic field of 0.1 T. The arrow pointed Mg content (x) for each $M(T)$ graph are inferred from EDS analysis. The olive coloured straight lines above and below the point of inflection of $M(T)$ data for for $x = 1.11$ and $x = 1.23$ shows the scheme for inferring the Curie temperature. Thus obtained Curie temperatures and Mg content phase diagram is presented in the inset. The black $\star$ represents the Curie temperature inferred from the tangents intersection scheme for single crystalline $Ce_{1.66}Mg_{1.34}Co_9$ sample on the $M(T)$ data measured along the hard axis of the plate.

The substitution of Mg for Ce changes a Pauli-paramagnet ($CeCo_3$) into a ferromagnet that has T_C increase with Mg content. The most likely reason for this is associated with valency and band filling. In $CeCo_3$, the Ce is essentially non-moment bearing; this implies a Ce^{4+} valency. As Mg^{2+} is added, there will be a clear change in band filling that most likely leads to Stoner-type magnetism associated with the Co 3-d bands. Further work, both computational and experimental will be needed to better appreciate the origin of the observed ferromagnetism.

Figure 11 shows the magnetic hysteresis curves of various polycrystals along with observed coercivity fields at 50 K (inset). The coercivity field increases with Mg content, becomes maximum (~ 0.35 T) for $x = 0.82$ and then decreases. The observation of coercivity is consistent with the axial nature of the magnetic anisotropy as will be detailed below. The abruptly increased coercivity for $x = 0.82$ and spontaneous magnetization for $x = 1.11$ magnesium containing phases were reproduced in multiple samples. It should be noted that differing saturation values for differing x are most likely due to non-random distribution of grains in these as-cast samples. In addition, the non-saturating behaviour of the $x = 1.35$ sample indicates either the presence of the preferred orientations of the grains with their hard axis along the applied field or presence of some anisotropic magnetic impurity in the sample. The former argument can be easily visualized in $M(T)$ data as $x = 1.35$ polycrystalline sample and single

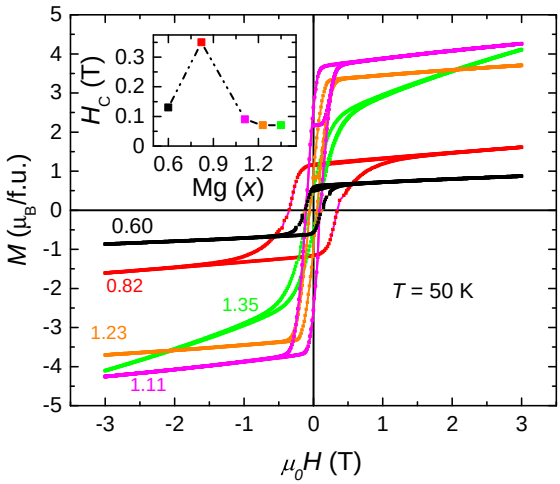

Figure 11. Magnetic hysteresis loop of various annealed polycrystalline $Ce_{3-x}Mg_xCo_9$ samples at 50 K. The values of Mg content are from EDS analysis. The inset shows the variation of the observed coercivity fields of the samples as a function of Mg content.

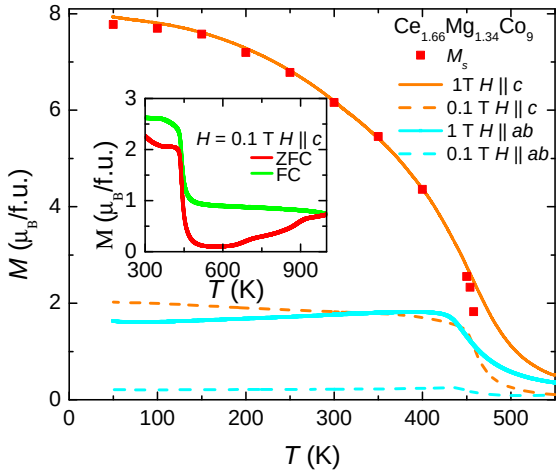

Figure 12. Anisotropic temperature dependent magnetization for $Ce_{1.66}Mg_{1.34}Co_9$ at various applied fields and directions. Dashed lines are for $H = 0.1$ T an solid lines are for $H = 1.0$ T. Individual data points (red squares) are spontaneous magnetization, M_S inferred from *M(H)* isotherms. The inset shows the zero field cooled (ZFC) and field cooled (FC) magnetization data along the easy axis of magnetization to temperature above the sample decomposition point.

crystalline $Ce_{1.66}Mg_{1.34}Co_9$ *M(T)* data along the hard axis are almost identical in nature as shown in FIG. 10. The fact that as-cast samples show coercivity is promising for the development of permanent magnets out of this system.

Our single crystal sample can provide further insight into this system's promise as a permanent magnet material. FIG. 12 shows the temperature dependence of the magnetization parallel and perpendicular to the c-axis of the single crystal of $Ce_{1.66}Mg_{1.34}Co_9$ up to 550 K. The c-

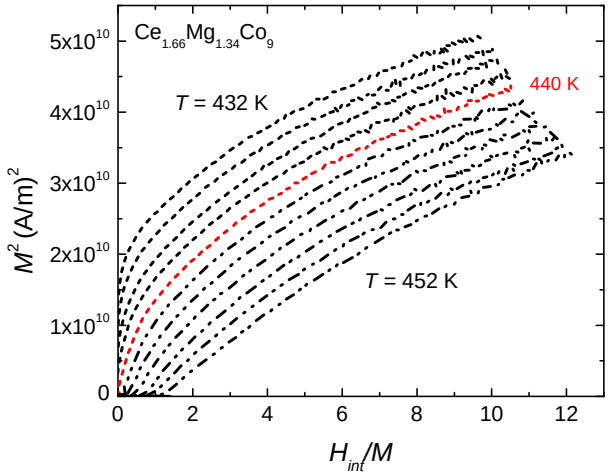

Figure 13. Arrott plot for a $Ce_{1.66}Mg_{1.34}Co_9$ single crystal within the temperature range of 432 K to 452 K at a step of 2 K between adjacent curves. The Curie temperature is determined to be 440 K.

axis is the easy axis of magnetization and the saturation magnetization at low temperature is 8 μ_B/f.u. The spontaneous magnetization data points for $Ce_{1.66}Mg_{1.34}Co_9$, represented with red squares, are obtained by the Y-intercept of linear fitting of the high field *M(H)* data (>1.5 T) in the first quadrant. No hysteresis was observed in the *M(H)* loops. The absence of hysteresis in *M(H)* isotherms measured in single crystals is due to absence of grain boundaries, defects and impurity atoms capable of pinning of the ferromagnetic domains. When measurements were performed up to 1000 K, we noticed a non-reproducibility of the results as shown in the inset of FIG. 12. Thermo-gravimetric analysis (not shown here) showed evidence for a decomposition of the samples, this degradation was not observed when limiting the measurements to a maximum temperature of 550 K.

An Arrott plot with several isotherms near the Curie temperature is shown in FIG. 13. The internal magnetic field H_{int} was determined using the relation $H_{int} = H_{app} - N * M$, where H_{app} is the applied field, N is the demagnetization factor which is experimentally determined along the easy axis ($N_c = 0.78$) [12, 13] and M is the magnetization. The Arrott curves are not linear indicating $Ce_{1.66}Mg_{1.34}Co_9$ does not follow the mean field theory. The Curie temperature of $Ce_{1.66}Mg_{1.34}Co_9$ is 440 K since Arrott curve corresponding to 440 K passes through the origin. This is comparable with the values of T_C obtained from polycrystals of similar composition (see inset of FIG. 10).

The magnetocrystalline anisotropy field was determined to be $\sim$ 10 T (T = 2 K) and $\sim$ 6 T (T = 300 K) for a $Ce_{1.66}Mg_{1.34}Co_9$ single crystalline sample, as shown in FIG. 14. The anisotropy field was determined by the linear extrapolation of the observed moment along the plane up to the saturation moment.

The anisotropy energy was quantified by using the

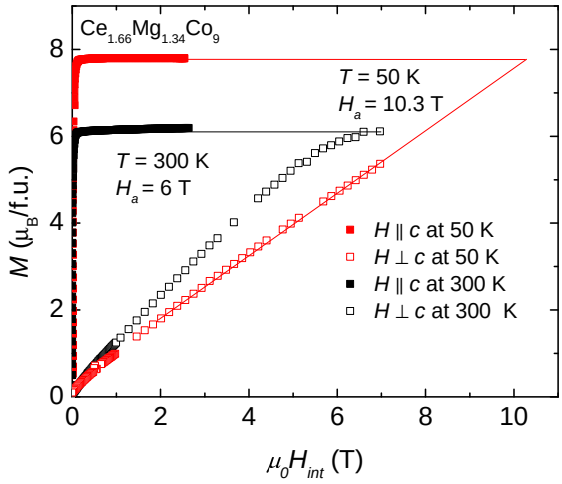

Figure 14. Anisotropic field dependent magnetization of $Ce_{1.66}Mg_{1.34}Co_9$ at 50 K ($H_a \approx 10\ T$) and 300 K ($H_a \approx 6$ T).

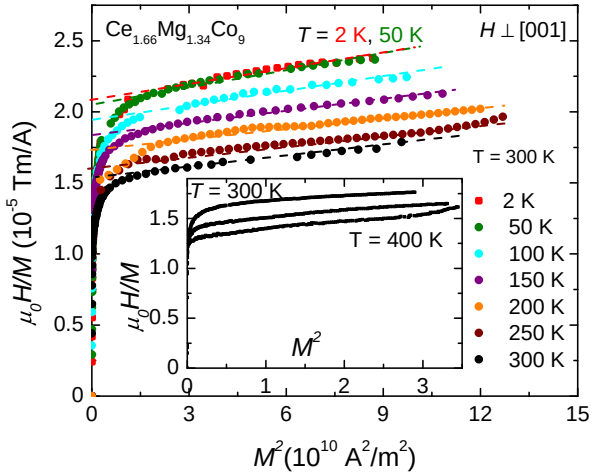

Figure 15. Sucksmith-Thompson plot for $Ce_{1.66}Mg_{1.34}Co_9$ to obtain anisotropy constants K_1 and K_2. The field dependent magnetization data were measured up to 7 T along the hard axis of magnetization. The dotted straight lines are the linear fit to $\frac{\mu_0 H}{M}$ at high field magnetization data to obtain the intercepts and slopes of the isotherms. The inset shows the Sucksmith-Thompson plots for VSM data measured along hard axis ($H \perp [001]$) up to 3 T field. K_1 and K_2 obtained by VSM data were matched to MPMS data at 300 K.

Sucksmith-Thompson plot for field dependent magnetization data along the plane as shown in FIG. 15. In the Sucksmith-Thompson plot, the ratio of magnetizing field with hard axis magnetization data is related to the anisotropy constants K_1 and K_2, saturation magnetization M_s and hard axis magnetization ($M_\perp$) as shown in equation (1)[17, 18].

$$\frac{\mu_0 H}{M_\perp} = \frac{2K_1}{M_s^2} + \frac{4K_2}{M_s^4} M_\perp^2 \qquad (1)$$

The intercept of the Sucksmith-Thompson plot gives

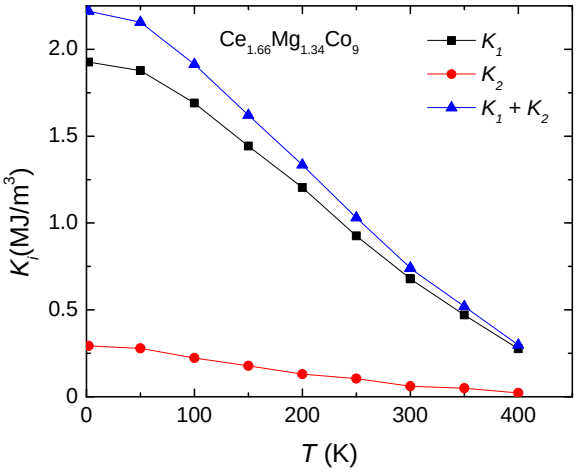

Figure 16. Temperature dependent anisotropy energy constants for $Ce_{1.66}Mg_{1.34}Co_9$. The anisotropy constants were determined from the Sucksmith-Thompson plot. The K_1 and K_2 values up to 300 K were measured using MPMS and higher temperature data are measured using VSM.

the anisotropy constant K_1 and slope gives the anisotropy constant K_2. FIG. 16 shows the temperature variation of the measured anisotropy constants. There was a slight mismatch ($< 2\%$) in the anisotropies data above and below the 300 K obtained from VSM and MPMS data. The VSM data were scaled to MPMS data at 300 K since slope of Sucksmith-Thompson plot are better determined with higher applied field. Here the total anisotropy energy of $Ce_{1.66}Mg_{1.34}Co_9$ is determined to be 2.2 MJ/m^3. Such high anisotropy energy density makes the $Ce_{1.66}Mg_{1.34}Co_9$ as a potential candidate for permanent magnet applications.

V. CONCLUSIONS

We investigated the effect of Mg substitution into the Ce_3Co_9 (e.g. $CeCo_3$) binary phase where Mg partially replaces the Ce atom on the $6c$ crystallographic site giving rise to the $Ce_{3-x}Mg_xCo_9$ solid solution for $0 \leq x \lesssim 1.4$. The substituted Mg induces ferromagnetism; the Curie temperature of the solid solution increases with higher content of Mg and becomes maximum (450 K) for Mg content $x = 1.35$. The magnetic anisotropy was determined for a self-flux grown $Ce_{1.66}Mg_{1.34}Co_9$ single crystal. The uniaxial-anisotropy field was determined to be $\sim$ 10 T at 2 K and $\sim$ 6 T at 300 K. The anisotropy energy density was determined to be 2.2 MJ/m^3 at 2 K. With these observed magnetic properties, $Ce_{3-x}Mg_xCo_9$ solution shows a potential to be used as a permanent magnet.

VI. ACKNOWLEDGEMENTS

We would like to thank Dr. T. Kong for useful discussions. Dr. Warren Straszheim is acknowledged for doing SEM on various samples. This research was supported by the Critical Materials Institute, an Energy Innovation Hub funded by the U.S. Department of Energy, Office of Energy Efficiency and Renewable Energy, Advanced Manufacturing Office. Q.L. is supported by the office of Basic Energy Sciences, Materials Sciences Division, U.S. DOE. This work was performed at the Ames Laboratory, operated for DOE by Iowa State University under Contract No. DE-AC02-07CH11358.

[1] G. B. Haxel, J. B. Hedrick, and G. J. Orris, "Rare earth elementscritical resources for high technology," U.S. Geological Survey Fact Sheet 087-02 (2002).

[2] Pradyot Patnaik, *Handbook of inorganic chemicals* (McGraw-Hill, 2003).

[3] Feng Xie, Ting An Zhang, David Dreisinger, and Fiona Doyle, "A critical review on solvent extraction of rare earths from aqueous solutions," Miner. Eng. **56**, 10 – 28 (2014).

[4] Arjun K. Pathak, Mahmud Khan, Karl A. Gschneidner, Ralph W. McCallum, Lin Zhou, Kewei Sun, Kevin W. Dennis, Chen Zhou, Frederick E. Pinkerton, Matthew J. Kramer, and Vitalij K. Pecharsky, "Cerium: An unlikely replacement of dysprosium in high performance ndfeb permanent magnets," Advanced Materials **27**, 2663–2667 (2015).

[5] RV Denys, AB Riabov, R Černỳ, IV Koval'chuk, and I Yu Zavaliy, "New $CeMgCo_4$ and Ce_2MgCo_9 compounds: Hydrogenation properties and crystal structure of hydrides," J. Solid State Chem. **187**, 1–6 (2012).

[6] V.V. Shtender, R.V. Denys, V. Paul-Boncour, I.Yu. Zavaliy, Yu.V. Verbovytskyy, and D.D. Taylor, "Crystal structure, hydrogen absorption-desorption behavior and magnetic properties of the $Nd_{3-x}Mg_xCo_9$ alloys," J. Alloys Compd. **695**, 1426 – 1435 (2017).

[7] M.I. Bartashevich, K. Koui, T. Goto, M. Yamaguchi, I. Yamamoto, and F. Sugaya, "Magnetic properties of $NdCo_3$ and its γ-phase hydride $NdCo_3H_{4.1}$," J. Alloys Compd. **202**, 7–12 (1993).

[8] Paul C. Canfield and Ian R. Fisher, "High-temperature solution growth of intermetallic single crystals and quasicrystals," J. Cryst. Growth **225**, 155 – 161 (2001).

[9] H. Okamoto, "Ce-co phase diagram, asm alloy phase diagrams database, p. villars, editor-in-chief; h. okamoto and k. cenzual, section editors," Ce-Co Phase Diagram, ASM Alloy Phase Diagrams Database, P. Villars, editor-in-chief; H. Okamoto and K. Cenzual, section editors (1990).

[10] A. C. Larson and R. B. Von Dreele, *General Structure Analysis System (GSAS)*, Los Alamos National Laboratory Report LAUR 86-748 (2004).

[11] Brian H. Toby, "*EXPGUI*, a graphical user interface for *GSAS*," Journal of Applied Crystallography **34**, 210–213 (2001).

[12] Tej N. Lamichhane, Valentin Taufour, Srinivasa Thimmaiah, David S. Parker, Sergey L. Bud'ko, and Paul C. Canfield, "A study of the physical properties of single crystalline Fe_5B_2P," J. Magn. Magn. Mater. **401**, 525 – 531 (2016).

[13] Tej N. Lamichhane, Valentin Taufour, Morgan W. Masters, David S. Parker, Udhara S. Kaluarachchi, Srinivasa Thimmaiah, Sergey L. Bud'ko, and Paul C. Canfield, "Discovery of ferromagnetism with large magnetic anisotropy in zrmnp and hfmnp," Appl. Phys. Lett. **109**, 092402 (2016), http://dx.doi.org/10.1063/1.4961933.

[14] A. Jesche, M. Fix, A. Kreyssig, W. R. Meier, and P. C. Canfield, "X-ray diffraction on large single crystals using a powder diffractometer," Philos. Mag. **96**, 2115–2124 (2016), http://dx.doi.org/10.1080/14786435.2016.1192725.

[15] R. Lemair, "Magnetic properties of the lntermetallic compounds of cobalt with the rare earth metals and yttrium," Cobalt **33**, 201–211 (1966).

[16] K.H.J. Buschow, "Magnetic properties of $CeCo_3$, Ce_2Co_7 and $CeNi_3$ and their ternary hydrides," Journal of the Less Common Metals **72**, 257 – 263 (1980).

[17] W. Sucksmith and J. E. Thompson, "The magnetic anisotropy of cobalt," Proceedings of the Royal Society of London A: Mathematical, Physical and Engineering Sciences **225**, 362–375 (1954), http://rspa.royalsocietypublishing.org/content/225/1162/362.full.pdf

[18] Valentin Taufour, Srinivasa Thimmaiah, Stephen March, Scott Saunders, Kewei Sun, Tej Nath Lamichhane, Matthew J. Kramer, Sergey L. Bud'ko, and Paul C. Canfield, "Structural and Ferromagnetic Properties of an Orthorhombic Phase of MnBi Stabilized with Rh Additions," Phys. Rev. Applied **4**, 014021 (2015).